

# Melting Experiments on Fe-O-H: Evidence for Eutectic Melting in Fe-FeH and Implications for Hydrogen in the Core

Oka Kenta<sup>1</sup>, Tagawa Shoh<sup>2</sup>, Hirose Kei<sup>2</sup>, and Ohishi Yasuo<sup>3</sup>

<sup>1</sup>Univ. Tokyo

<sup>2</sup>Tokyo Institute of Technology

<sup>3</sup>Japan Synchrotron Radiation Research Institute

November 16, 2022

## Abstract

We examined liquidus phase relations in Fe-O+/-H at  $\sim 40$  and  $\sim 150$  GPa, and subsolidus phase equilibria in Fe-FeH. While it has been speculated that Fe and FeH form continuous solid solution to core pressures, our experiments show the coexistence of the H-poor hcp and H-rich fcc phases in the Fe-FeH system. Considering higher melting temperature of stoichiometric FeH than that of Fe-FeH, it indicates eutectic melting between Fe and FeH. It is consistent with the liquidus phase diagram in Fe-O-H, which implies the Fe-FeH binary eutectic liquid composition of FeH<sub>0.42</sub> at  $\sim 40$  GPa. We estimated the outer core liquid composition to be Fe + 2.9-5.2% O + 0.03-0.32% H + 0-3.4% Si + 1.7% S by weight, based on the liquidus phase relations, solid-liquid partitioning, and outer/inner core densities and velocities, indicating that O and either H or Si are important core light elements.

# Melting Experiments on Fe-O-H: Evidence for Eutectic Melting in Fe-FeH and Implications for Hydrogen in the Core

Kenta Oka<sup>1</sup>, Shoh Tagawa<sup>1,2</sup>, Kei Hirose<sup>1,2</sup>, and Yasuo Ohishi<sup>3</sup>

<sup>1</sup>Department of Earth and Planetary Science, The University of Tokyo, Bunkyo, Tokyo, Japan

<sup>2</sup>Earth-Life Science Institute, Tokyo Institute of Technology, Meguro, Tokyo, Japan

<sup>3</sup>Japan Synchrotron Radiation Research Institute, SPring-8, Sayo, Hyogo, Japan

## Key Points:

- We examined the liquidus phase relations and solid/liquid partitioning in the Fe-O±H system at ~40 GPa and ~150 GPa.
- Eutectic melting between Fe and FeH is indicated from the liquidus phase relations in Fe-O-H and the subsolidus phase equilibria in Fe-H.
- The outer core may include 2.9–5.2 wt% O, 0.03–0.32 wt% H, 0–3.4 wt% Si, and 1.7 wt% S.

**Abstract** We examined liquidus phase relations in Fe-O±H at ~40 and ~150 GPa, and subsolidus phase equilibria in Fe-FeH. While it has been speculated that Fe and FeH form continuous solid solution to core pressures, our experiments show the coexistence of the H-poor hcp and H-rich fcc phases in the Fe-FeH system. Considering higher melting temperature of stoichiometric FeH than that of Fe-FeH, it indicates eutectic melting between Fe and FeH. It is consistent with the liquidus phase diagram in Fe-O-H, which implies the Fe-FeH binary eutectic liquid composition of FeH<sub>0.42</sub> at ~40 GPa. We estimated the outer core liquid composition to be Fe + 2.9–5.2% O + 0.03–0.32% H + 0–3.4% Si + 1.7% S by weight, based on the liquidus phase relations, solid-liquid partitioning, and outer/inner core densities and velocities, indicating that O and either H or Si are important core light elements.

**Plain Language Summary** We have investigated the liquidus and subsolidus phase relations in the Fe-O±H and Fe-H systems, respectively, at high pressures in a laser-heated diamond-anvil cell. The solid-liquid partition coefficient of H was also determined. While it is known that Fe and stoichiometric FeH form continuous solid solution at least to ~20 GPa, our experiments on the Fe-O-H ternary and Fe-H binary systems performed above 40 GPa consistently suggested eutectic melting between Fe and FeH with eutectic liquid

35 composition of  $\text{FeH}_{0.42}$ . We explored the possible range of the liquid core composition,  
36 which should be 1) within the liquidus field of Fe to crystallize the dense inner core, 2)  
37 compatible with seismological observations of the outer core, and 3) in equilibrium with  
38 the inner core solid that explains the observed density and velocities. The results indicate  
39 that the outer core is rich in O and either H or Si, supporting the delivery of a large amount  
40 of water to the Earth found in recent planet formation theories and its sequestration into  
41 the metallic core that is inferred from metal-silicate partitioning data.

## 42 **1. Introduction**

43 The Earth's core should contain more than one light impurity elements (see recent reviews  
44 by Li & Fei, 2014 and Hirose et al., 2021). Both O and H can be important core light  
45 elements because the density and sound velocity observed in the outer core are compatible  
46 with the presence of O (Badro et al., 2014) and H (Umemoto & Hirose, 2015, 2020).  
47 Recent planet formation models suggested that 10 to 100 times ocean mass of water may  
48 have been brought to the Earth during its accretion (e.g., Raymond et al., 2007; Walsh et  
49 al., 2011). The chemical reaction of solar-nebula-type H-rich proto-atmosphere with FeO  
50 could have been another source of water (Ikoma & Genda, 2006; Olson & Sharp, 2019).  
51 It is likely that most of  $\text{H}_2\text{O}$  was once dissolved into a magma ocean, and H and O were  
52 incorporated into core-forming metals during their segregation from silicate (Tagawa,  
53 Sakamoto et al., 2021; Li et al., 2020; Yuan & Steinle-Neumann, 2020).

54 Liquidus phase relations of Fe alloy systems, in particular the liquidus field of Fe (a  
55 compositional range of liquids that first crystallize Fe), constrain the outer core  
56 composition (e.g., Yokoo et al., 2019; Hasegawa et al., 2021). When O and H are two  
57 major core light elements, the liquid core should not crystallize FeO nor FeH but Fe at  
58 the inner core boundary (ICB), otherwise the denser solid inner core is not formed. In  
59 order to understand the liquidus phase relations in the Fe-O-H system, the knowledge on  
60 the relevant binary systems is helpful. Previous high-pressure experiments demonstrated  
61 that O concentration in the Fe-FeO eutectic liquid increases with increasing pressure  
62 (Morard et al., 2017; Oka et al., 2019). The recent study by Oka and others based on  
63 experiments to 204 GPa estimated 15 wt% O in the Fe-FeO binary eutectic liquid at ICB.  
64 On the other hand, earlier high-pressure melting experiments on the Fe( $\pm$ Ni)-H system  
65 were limited to 20 GPa (Sakamaki et al., 2009; Imai, 2013; Shibazaki et al., 2014) because  
66 of a technical difficulty in dealing with hydrogen. Fukai (1992) speculated a continuous  
67 solid solution between Fe and stoichiometric FeH to megabar pressure, but it has been  
68 verified only to  $\sim$ 20 GPa (Imai, 2013; Shibazaki et al., 2014).

69 In this study, we have carried out melting experiments on the Fe-O±H system at ~40 GPa  
70 and ~150 GPa. Our results on Fe-O-H suggest that Fe-FeH is an eutectic system, which  
71 contradicts the phase diagram supposed by Fukai (1992) but is supported by our  
72 additional experiment on an Fe-H alloy. Our findings of 1) eutectic melting between Fe  
73 and FeH, 2) liquidus phase relations in the Fe-O-H system, and 3) the solid-liquid  
74 partitioning of H help to constrain concentrations of O, H, and other light elements in the  
75 outer core.

## 76 **2. Results**

77 We have examined the phase relations in the Fe-O±H and Fe-FeH systems on the basis  
78 of high-pressure and -temperature ( $P$ - $T$ ) experiments using laser-heated diamond-anvil  
79 cell (DAC) techniques, combined with in-situ synchrotron X-ray diffraction (XRD)  
80 measurements and ex-situ textural and compositional characterizations using electron  
81 microprobes (see Experimental Methods in the Supporting Information).

### 82 **2.1. Melting in Fe-O±H**

83 A total of six separate melting experiments were carried out at ~40 GPa and ~150 GPa  
84 (runs #A1–A6 in [Table S1](#)). For all runs, we performed synchrotron XRD measurements  
85 and subsequent microprobe observations on recovered samples. In run #A4, while the  
86 intense peaks from hcp Fe were present before heating, they were almost lost and  
87 alternatively a diffuse signal characteristic of liquid was observed around 12 degrees of  
88 two-theta angle upon heating to 2370 K ([Figure 1a](#)). Upon quenching temperature, the  
89 peaks of fcc FeH<sub>*x*</sub> ( $x = 0.31$ ) appeared from liquid. The XRD pattern obtained at ~12 μm  
90 away from the center of a laser-heated spot included strong peaks from rhombohedrally-  
91 distorted B1 FeO and hcp FeH<sub>*x*</sub> ( $x = 0.24$ ).

92 This sample was recovered from a DAC, and in its cross section, there was a chemically  
93 homogeneous area with a non-stoichiometric composition at the center, which represents  
94 a quenched liquid ([Figures 2a, b](#)). The earlier DAC experiments by Hirose et al. (2019)  
95 and Tagawa, Sakamoto et al. (2021) demonstrated that the H content in FeH<sub>*x*</sub> crystals  
96 formed from liquid upon quenching temperature closely represents that of Fe-H liquid.  
97 We therefore consider that Fe-O-H liquids in the present experiments were fully quenched  
98 into a mixture of solid FeH<sub>*x*</sub> and FeO. The proportion of FeO was obtained from the  
99 EPMA analysis of O concentration in the quenched liquid. The remaining phase  
100 proportion of FeH<sub>*x*</sub> and its H concentration  $x$  that was estimated from its lattice volume  
101 in XRD patterns give 0.49 wt% H in the Fe-O-H liquid ([Table S1](#)). Next to the liquid pool,

102 electron microprobe images showed a couple of single-phase layers of Fe and FeO  
103 (Figures 2a, b). According to the XRD observations, the Fe layer was solid FeH<sub>0.24</sub> (Fe +  
104 0.43 wt% H) before it lost hydrogen during decompression (Figure 1a). The liquid was in  
105 direct contact with the FeO layer or in some place with the FeH<sub>0.24</sub> layer, indicating that  
106 both FeO and FeH<sub>0.24</sub> are the liquidus phases of the Fe-O-H liquid formed in run #A4.  
107 The outside of these liquidus phase layers was not melted during laser heating. Runs #A1–  
108 A3 were carried out around 40 GPa in a similar manner with changing the Fe/H<sub>2</sub>O ratio  
109 in the starting materials (Table S1). The liquids included 0.1–0.4 wt% C except 1.7 wt%  
110 C in run #A1.

111 In runs #A5 and #A6 performed at ~150 GPa, liquids were crystallized into the hcp phase  
112 upon quenching temperature to 300 K, which included minimal amounts of H (<0.04  
113 wt%) (Table S1). The EPMA data showed 10.4–13.0 wt% O and 0.9–3.7 wt% C in  
114 quenched liquids, indicating they were Fe-O±C liquids. The liquid Fe-13.0wt%O-  
115 0.9wt%C obtained in run #A5 coexisted with solid Fe, giving the lower bound for O  
116 concentration in the Fe-FeO binary eutectic liquid at 147 GPa (Figure S1). It helps to  
117 constrain the change in the eutectic liquid composition in the Fe-FeO system with  
118 increasing pressure, which was previously estimated only with a single datum point above  
119 50 GPa in Oka et al. (2019).

## 120 2.2. Subsolidus Phase Relations in Fe-FeH

121 An additional experiment was carried out on the Fe-FeH binary system at 62 GPa (run  
122 #B in Table S2) (see Experimental Methods in the Supporting Information).  
123 Stoichiometric dhcp FeH was synthesized by heating to <1000 K at 8 GPa. The excess  
124 molecular H<sub>2</sub> in the sample chamber was lost to a neighboring rhenium gasket to form  
125 ReH<sub>x</sub> upon compression to 23 GPa (Scheler et al., 2011). The dhcp FeH was then  
126 transformed into fcc FeH<sub>0.87</sub> by reheating to ~1000 K for 3 min at 44 GPa (Figure 1b).  
127 Subsequently this sample was further compressed to ~60 GPa and reheated for ~40 min  
128 at each temperature. At 1640 K and 62 GPa, while the sample was still fcc FeH<sub>x</sub>, its H  
129 content *x* reduced from 0.87 to 0.77. At higher temperature of 1830 K, it further  
130 diminished to 0.69, and at the same time hcp FeH<sub>0.21</sub> appeared. The sample melted at a  
131 slightly higher temperature.

## 132 3. Discussion

### 133 3.1. Eutectic Melting in Fe-FeH and the Liquidus Phase Relations in Fe-O-H

134 The high-pressure phase relations in the Fe-H system have been speculated by Fukai  
135 (1992), suggesting 1) a continuous solid solution between Fe and FeH and 2) an eutectic  
136 point located at  $\text{FeH}_x$  ( $x > 1$ ). The multi-anvil experiments by Imai (2013) and Shibazaki  
137 et al. (2014) reported the melting and subsolidus phase relations in the Fe-FeH( $\pm$ Ni)  
138 system to 15–20 GPa, which are consistent with the phase diagram supposed by Fukai  
139 (1992). In contrast, run #B in the present study demonstrated the coexistence of hcp  
140  $\text{FeH}_{0.21}$  and fcc  $\text{FeH}_{0.69}$  at 62 GPa and 1830 K (Figure 1b), indicating a gap in solid  
141 solution right below the melting temperature. In addition, earlier experiments  
142 demonstrated that stoichiometric FeH does not melt, at least to 2600 K at this pressure  
143 (Tagawa, Gomi et al., 2021). These suggest eutectic (not peritectic) melting between the  
144 H-poor hcp and H-rich fcc phases in the Fe-FeH system. Indeed, the eutectic melting is a  
145 natural consequence of the facts that 1) Fe and FeH end-members adopt different crystal  
146 structures of hcp (Komabayashi et al., 2009) and fcc (Kato et al., 2020; Thompson et al.,  
147 2018; Isaev et al., 2007), respectively and 2) stoichiometric FeH melts at temperature  
148 much higher than that for  $\text{FeH}_{0.21-0.69}$ . The presence of the gap in solid solution between  
149 hcp Fe and fcc FeH and the resulting eutectic melting are likely to be hold to Earth's inner  
150 core conditions (Tagawa, Gomi et al., 2021).

151 The compositions of liquids obtained at  $\sim$ 40 GPa in runs #A1–A4 are plotted in the Fe-  
152 O-H ternary diagram (Figure 3a). The liquid compositions found in runs #A2 and #A3  
153 should be within the liquidus field of FeO, and that in run #A4 is on the Fe + FeO cotectic  
154 line (showing the liquid compositions coexisting with both Fe and FeO). Considering the  
155 eutectic point in the Fe-FeO binary (Figure S1), the position of the Fe + FeO cotectic line  
156 is tightly constrained. Figure 3a illustrates the liquidus phase relations in the Fe-O-H  
157 system. The liquidus field of FeO extends close to the Fe-FeH side, and the ternary  
158 peritectic (or possibly eutectic) point should be located at the H-rich portion of the phase  
159 diagram. It suggests the presence of the Fe-FeH binary eutectic point at  $\text{FeH}_{0.42}$  (Fe + 0.75  
160 wt% H) in agreement with a gap in solid solution between hcp  $\text{FeH}_{0.21}$  and fcc  $\text{FeH}_{0.69}$   
161 right below the melting temperature as observed in run #B.

162 The Fe-FeH binary eutectic liquid composition may change little with increasing pressure  
163 because the high  $P$ - $T$  experiments performed by Tagawa, Gomi et al. (2021) showed that  
164 the temperature/pressure slope of the melting curve of stoichiometric FeH could be  
165 similar to that of Fe at  $>$ 40 GPa. On the other hand, the present results on the Fe-FeO  
166 system as well as earlier experiments (Seagle et al., 2008; Oka et al., 2019) and  
167 thermodynamic calculations (Komabayashi, 2014) demonstrate that O concentration in  
168 the Fe-FeO binary eutectic liquid increases to 15 wt% with increasing pressure to 330

169 GPa. The Fe-O±C liquids obtained in runs #A5 and #A6 verify the pressure evolution of  
170 the Fe-FeO eutectic liquid composition (the composition of liquid that coexists with both  
171 Fe and FeO) in the presence of <1 wt% and ~3 wt% C, respectively (Figure S1). By taking  
172 the positions of the Fe-FeO and Fe-FeH binary eutectic points into account, we suppose  
173 the Fe-O-H ternary liquidus phase relations at the ICB pressure in Figure 3b.

### 174 3.2. Possible Outer Core Liquid Composition

175 Since the outer core crystallizes the dense inner core at the ICB, the liquid composition  
176 should be within the liquidus field of Fe at 330 GPa (Figure 3b). It has been demonstrated  
177 by earlier experiments on ternary Fe alloy systems containing two light elements—Fe-Si-  
178 S (Tateno et al., 2018), Fe-S-O (Yokoo et al., 2019), Fe-Si-C (Hasegawa et al., 2021), and  
179 Fe-C-O (Sakai et al., 2021)—that the ternary eutectic point is located close to the tie line  
180 between the eutectic points in relevant binary systems; in other words, the liquidus field  
181 of Fe (such as a colored area in Figure 3b) in these ternary systems can be approximated  
182 by linear interpolation between the eutectic liquid compositions in relevant binary  
183 systems. This may be extended to the Fe-O-H-Si-S system that we consider for the liquid  
184 outer core; the liquidus field of Fe could be estimated from the four relevant binary  
185 eutectic compositions at 330 GPa; Fe with 15 wt% O (Figure S1), 0.75 wt% H (Figure  
186 3b), 8 wt% Si (Hasegawa et al., 2021), or 5 wt% S (Mori et al., 2017).

187 We estimate the possible range of the outer core liquid composition based on three  
188 independent constraints (Hirose et al., 2021). First, 1) it must account for the density and  
189 P-wave velocity observed in the outer core (Umemoto & Hirose, 2020). Here we consider  
190  $T_{\text{ICB}} = 5800$  K and  $6280$  K, which correspond to  $T_{360\text{GPa}} = 6000$  K and  $6500$  K,  
191 respectively, when assuming isentropic temperature profiles with Grüneisen parameter  $\gamma$   
192  $= 1.5$  (Vočadlo et al., 2003) (these are the conditions at which the possible inner core  
193 composition was examined by Wang et al., 2021). Also, 2) the liquid core composition  
194 should be within the liquidus field of Fe in the Fe-O-H-Si±1.7wt%S system at the ICB  
195 pressure. Geochemical and cosmochemical estimates have consistently proposed ~2 wt%  
196 S in the core (Dreibus & Palme, 1996; McDonough, 2014), and here we adopt 0 or 1.7  
197 wt% S in the outer core according to Dreibus & Palme. The colored portions in Figures  
198 4a–d indicate O, H, and Si concentrations in liquids Fe-O-H-Si±1.7wt%S, which meet  
199 these two constraints from 1) the outer core density and velocity and 2) the liquidus phase  
200 diagram at 330 GPa.

201 In addition, 3) the third constraint is from the possible inner core solid composition that  
202 was estimated in Fe-Si-S(-C) by Li et al. (2018) and in Fe-H-Si by Wang et al. (2021),

203 which explains the observed density, P-wave and S-wave velocities (Dziewonski &  
 204 Anderson, 1981; Kennett et al., 1995). Their calculations of  $\text{Fe}_{64-y}\text{Si}_y$  ( $y = 0, 4, \text{ and } 8$ ) and  
 205  $\text{Fe}_{60}\text{Si}_4\text{H}_z$  ( $z = 1, 2, 4, \text{ and } 8$ ) alloys demonstrated that the density ( $\rho$ ), P-wave ( $V_P$ ) and S-  
 206 wave velocities ( $V_S$ ) of Fe alloys are written as;  $\rho = -0.105y - 0.039z + 13.639(5)$ ,  $V_P = -$   
 207  $0.001y - 0.034z + 11.559(128)$ , and  $V_S = -0.061y - 0.053z + 4.108(154)$  at  $T_{360\text{GPa}} = 6500$   
 208 K, and  $\rho = -0.104y - 0.038z + 13.682(48)$ ,  $V_P = 0.001y - 0.019z + 11.619(110)$ , and  $V_S =$   
 209  $-0.060y - 0.033z + 4.229(140)$  at  $T_{360\text{GPa}} = 6000$  K. The inner core may include 1.4 wt%  
 210 S, which is calculated from the 1.7 wt% S in the outer core and the solid/liquid partition  
 211 coefficient of S,  $D_S$  (solid/liquid) = 0.8 by weight at 330 GPa (Alfè et al., 2002; Yokoo et  
 212 al., 2019). Since Wang et al. (2021) mentioned that the effects of S and Si on the density  
 213 and sound velocities are similar to each other, we consider that the effect of S is the same  
 214 as that of Si. O is not partitioned into solid Fe and thus not considered in the inner core  
 215 (Alfè et al., 2002; Ozawa et al., 2010). With these relations, we obtain the possible ranges  
 216 of the inner core composition in the Fe-H-Si $\pm$ 1.4wt%S system, depending on temperature.  
 217 It gives the liquid outer core composition based on the solid/liquid partition coefficients  
 218  $D_H = 0.89$  (this study, Table S1) and  $D_{\text{Si}}$  (solid/liquid) = 1.0 by weight (Alfè et al., 2002;  
 219 Kuwayama & Hirose, 2004). The  $D_H = 0.89$  obtained in this study at 39 GPa is slightly  
 220 higher than 0.72–0.74 reported by earlier multi-anvil experiments at 15–20 GPa (Imai,  
 221 2013). The compositional ranges of liquids in equilibrium with the possible inner core  
 222 solid are illustrated by areas enclosed by black lines in Figures 4a–d.

223 The overlap between the colored area (constrained by the outer core density and velocity  
 224 and by the liquidus field of Fe) and the black enclosed area (constrained by the inner core  
 225 density and velocities) in Figures 4a–d indicates the possible compositional range for the  
 226 liquid outer core. It becomes smaller with 1.7 and 1.4 wt% S respectively in the outer and  
 227 inner core than in S-free cases. Possible liquid compositions are not found in the Fe-O-  
 228 H-Si-1.7wt%S system when  $T_{\text{ICB}} = 5800$  K ( $T_{360\text{GPa}} = 6000$  K) (Figure 4c). If  $T_{\text{ICB}} = 6280$   
 229 K ( $T_{360\text{GPa}} = 6500$  K), the outer core may include 2.9–5.2 wt% O, 0.03–0.32 wt% H, and  
 230 0–3.4 wt% Si and in addition to 1.7 wt% S. It suggests that O and either H or Si are  
 231 important light elements in the core, supporting the recent arguments that a large amount  
 232 of water was brought to the Earth during its accretion and mostly incorporated into core-  
 233 forming metals (Tagawa, Sakamoto et al., 2021; Li et al., 2020; Yuan & Steinle-Neumann,  
 234 2020). The range of the O content is still consistent with the recent estimate of <3.8 wt%  
 235 O in the outer core to explain the density jump across the ICB, which was based on the  
 236 experimentally-determined equations of state of liquid and solid Fe (Kuwayama et al.,  
 237 2020). Indeed,  $\sim 0.2$  wt.% C could be also present in the core (Fischer et al., 2020), but it  
 238 hardly decreases the present estimates of the core inventories of other light elements.

239 The  $T_{\text{ICB}} = 6280 \text{ K}$  ( $T_{360\text{GPa}} = 6500 \text{ K}$ ), however, corresponds to about 4600 K at the CMB  
240 when  $\gamma = 1.5$  (Vočadlo et al., 2003). It is much higher than the solidus temperatures of the  
241 pyrolitic and chondritic mantle materials at 135 GPa (Fiquet et al., 2010; Andraut et al.,  
242 2011; Nomura et al., 2014; Kim et al., 2020). It could therefore lead to extensive melting  
243 in the lowermost mantle, but seismology reveals the presence of partial melts only locally  
244 above the CMB at ultralow velocity zones. It is necessary to better constrain the core  
245 temperature to further explore the possible core composition (Hirose et al., 2021).

#### 246 **4. Conclusions**

247 We obtained the liquidus phase relations in the Fe-O-H ternary system at  $\sim 40 \text{ GPa}$  based  
248 on melting and subsolidus experiments on Fe-O $\pm$ H and Fe-H, respectively. While earlier  
249 studies reported that Fe and stoichiometric FeH form a continuous solid solution below  
250  $\sim 20 \text{ GPa}$  (Sakamaki et al., 2009; Imai, 2013; Shibazaki et al., 2014), our results indicated  
251 eutectic melting between Fe and FeH from the observations that 1) hcp Fe coexists with  
252 fcc FeH right below melting temperature, 2) stoichiometric FeH melts at temperature  
253 much higher than the melting temperature of FeH<sub>0.21–0.69</sub> (Tagawa, Gomi et al., 2021), and  
254 3) melting phase relations in the Fe-O-H ternary require the eutectic point in the Fe-FeH  
255 system. The Fe-FeH eutectic liquid composition is found to be FeH<sub>0.42</sub> (Fe + 0.75 wt%  
256 H) at  $\sim 40 \text{ GPa}$ . The present study combined with earlier experiments demonstrates that  
257 O concentration in the Fe-FeO binary eutectic liquid increases to 15 wt% at 330 GPa. On  
258 the other hand, pressure effect on the Fe-FeH eutectic liquid composition is likely small  
259 because the temperature/pressure slope of FeH may be comparable to that of Fe (Tagawa,  
260 Gomi et al., 2021). These allow us to extrapolate the liquidus phase relations in the Fe-  
261 O-H system to 330 GPa.

262 We estimated the possible range of the outer core liquid composition to be Fe + 2.9–5.2  
263 wt% O + 0–3.4 wt% Si + 0.03–0.32 wt% H + 1.7 wt% S, based on constraints from 1)  
264 the liquidus field of Fe (in order to crystallize the dense inner core), 2) the outer core  
265 density and velocity, and 3) the inner core density and velocities (the outer core  
266 composition is calculated from that of the inner core using the solid-liquid partition  
267 coefficients of light elements at ICB conditions). It indicates that O and either H or Si are  
268 important core light impurity elements, which supports recent arguments on the delivery  
269 of a large amount of water to the growing Earth and its incorporation into core metals for  
270 the most part.

#### 271 **Data Availability Statement**

272 Datasets for this research are found in [Tables S1](#) and [S2](#) available online (from  
273 <https://doi.org/10.5281/zenodo.5906236>).

## 274 **Acknowledgments**

275 We thank K. Yonemitsu for sample analyses with FIB, EDS, and FE-EPMA. This work  
276 was supported by the JSPS research grants 16H06285 and 21H04506 to K.H. XRD  
277 measurements were performed at BL10XU, SPring-8 (proposals no. 2016B0072,  
278 2019A0072, and 2019B0072).

## 279 **References**

- 280 Alfè, D., Gillan, M. J., & Price, G. D. (2002). Composition and temperature of the earth's  
281 core constrained by combining ab initio calculations and seismic data. *Earth and*  
282 *Planetary Science Letters*, *195*, 91–98.  
283 [https://doi.org/10.1016/S0012-821X\(01\)00568-4](https://doi.org/10.1016/S0012-821X(01)00568-4)
- 284 Andrault, D., Bolfan-Casanova, N., Nigro, G. Lo, Bouhifd, M. A., Garbarino, G., &  
285 Mezouar, M. (2011). Solidus and liquidus profiles of chondritic mantle: implication  
286 for melting of the Earth across its history. *Earth and Planetary Science Letters*, *304*,  
287 251–259. <https://doi.org/10.1016/j.epsl.2011.02.006>
- 288 Badro, J., Cote, A. S., & Brodholt, J. P. (2014). A seismologically consistent  
289 compositional model of Earth's core. *Proceedings of the National Academy of Science*  
290 *of the United States of America*, *111*, 7542–7545.  
291 <https://doi.org/10.1073/pnas.1316708111>
- 292 Dreibus, G., & Palme, H. (1996). Cosmochemical constraints on the sulfur content in the  
293 Earth's core. *Geochimica et Cosmochimica Acta*, *60*, 1125–1130.  
294 [https://doi.org/10.1016/0016-7037\(96\)00028-2](https://doi.org/10.1016/0016-7037(96)00028-2)
- 295 Dziewonski, A. M., & Anderson, D. L. (1981). Preliminary reference Earth model.  
296 *Physics of the Earth and Planetary Interiors*, *25*, 297–356.  
297 [https://doi.org/10.1016/0031-9201\(81\)90046-7](https://doi.org/10.1016/0031-9201(81)90046-7)
- 298 Fukai, Y. (1992). Some properties of the Fe-H system at high pressures and temperatures,  
299 and their implications for the Earth's core. In Y. Syono, M.H. Manghnani (Eds.), *High-*  
300 *pressure research: applications to Earth and planetary sciences* (Vol. 67, pp. 373–385).  
301 <https://doi.org/10.1029/GM067p0373>
- 302 Fischer, R. A., Cottrell, E., Hauri, E., Lee, K. K. M., & Le Voyer, M. (2020). The carbon  
303 content of Earth and its core. *Proceedings of the National Academy of Sciences of the*

304 *United States of America*, 117, 8743–8749.  
305 <https://doi.org/10.1073/pnas.1919930117>

306 Fiquet, G., Auzende, A. L., Siebert, J., Corgne, A., Bureau, H., Ozawa, H., & Garbarino,  
307 G. (2010). Melting of peridotite to 140 gigapascals. *Science*, 329, 1516–1518.  
308 <https://doi.org/10.1126/science.1192448>

309 Hasegawa, M., Hirose, K., Oka, K., & Ohishi, Y. (2021). Liquidus phase relations and  
310 solid-liquid partitioning in the Fe-Si-C system under core pressures. *Geophysical*  
311 *Research Letters*, 48, e2021GL092681. <https://doi.org/10.1029/2021GL092681>

312 Hirose, K., Wood, B., & Vočadlo, L. (2021). Light elements in the Earth’s core. *Nature*  
313 *Reviews Earth & Environment*, 2, 645–658. [https://doi.org/10.1038/s43017-021-](https://doi.org/10.1038/s43017-021-00203-6)  
314 00203-6

315 Ikoma, M., & Genda, H. (2006). Constraints on the mass of a habitable planet with water  
316 of nebular origin. *The Astrophysical Journal*, 648, 696. <https://doi.org/10.1086/505780>

317 Imai, T. (2013). *Crystal/melt partitioning under deep mantle conditions and melting*  
318 *phase relation in the system Fe-FeH* (PhD thesis). Tokyo Institute of Technology

319 Isaev, E. I., Skorodumova, N. V., Ahuja, R., Vekilov, Y. K., & Johansson, B. (2007).  
320 Dynamical stability of Fe-H in the Earth’s mantle and core regions, *Proceedings of the*  
321 *National Academy of Sciences of the United States of America*, 104, 9168–9171.  
322 <https://doi.org/10.1073/pnas.0609701104>

323 Kato, C., Umemoto, K., Ohta, K., Tagawa, S., Hirose, K., & Ohishi, Y. (2020). Stability  
324 of fcc phase FeH to 137 GPa. *American Mineralogist*, 105, 917–921.  
325 <https://doi.org/10.2138/am-2020-7153>

326 Kennett, B. L. N., Engdahl, E. R., & Buland, R. (1995). Constraints on seismic velocities  
327 in the Earth from traveltimes. *Geophysical Journal International*, 122, 108–124.  
328 <https://doi.org/10.1111/j.1365-246X.1995.tb03540.x>

329 Kim, T., Ko, B., Greenberg, E., Prakapenka, V., Shim, S. H., & Lee, Y. (2020). Low  
330 melting temperature of anhydrous mantle materials at the core-mantle boundary.  
331 *Geophysical Research Letters*, 47, 1–10. <https://doi.org/10.1029/2020GL089345>

332 Komabayashi, T. (2014). Thermodynamics of melting relations in the system Fe-FeO at  
333 high pressure: implications for oxygen in the Earth’s core. *Journal of Geophysical*  
334 *Research: Solid Earth*, 119, 4164–4177. <https://doi.org/10.1002/2014JB010980>

335 Komabayashi, T., Fei, Y., Meng, Y., & Prakapenka, V. (2009). In-situ X-ray diffraction  
336 measurements of the  $\gamma$ - $\epsilon$  transition boundary of iron in an internally-heated diamond  
337 anvil cell. *Earth and Planetary Science Letters*, 282, 252–257.  
338 <https://doi.org/10.1016/j.epsl.2009.03.025>

- 339 Kuwayama, Y., & Hirose, K. (2004). Phase relations in the system Fe-FeSi at 21 GPa.  
340 *American Mineralogist*, 89, 273–276. <https://doi.org/10.2138/am-2004-2-303>
- 341 Kuwayama, Y., Morard, G., Nakajima, Y., Hirose, K., Baron, A. Q. R., Kawaguchi, S. I.,  
342 et al. (2020). Equation of state of liquid iron under extreme conditions. *Physical*  
343 *Review Letters*, 124, 165701. <https://doi.org/10.1103/PhysRevLett.124.165701>
- 344 Li, J., & Fei, Y. (2014). Experimental constraints on core composition. In *Treatise on*  
345 *geochemistry* (2nd ed., Vol. 3, pp. 527–557). Amsterdam. Elsevier.  
346 <https://doi.org/10.1016/b978-0-08-095975-7.00214-x>
- 347 Li, Y., Vočadlo, & L., Brodholt, J. P. (2018). The elastic properties of hcp-Fe alloys under  
348 the conditions of the Earth's inner core. *Earth and Planetary Science Letters*, 493,  
349 118–127. <https://doi.org/10.1016/j.epsl.2018.04.013>
- 350 Li, Y., Vočadlo, L., Sun, T., & Brodholt, J. P. (2020). The Earth's core as a reservoir of  
351 water. *Nature Geoscience*, 13, 453–458. <https://doi.org/10.1038/s41561-020-0578-1>
- 352 McDonough, W. F. (2014). Compositional model for the Earth's core. In *Treatise on*  
353 *geochemistry* (2nd ed., Vol. 3, pp. 559–577). Amsterdam. Elsevier.  
354 <https://doi.org/10.1016/B978-0-08-095975-7.00215-1>
- 355 Morard, G., Andrault, D., Antonangeli, D., Nakajima, Y., Auzende, A. L., Boulard, E., et  
356 al. (2017). Fe–FeO and Fe–Fe<sub>3</sub>C melting relations at Earth's core–mantle boundary  
357 conditions: implications for a volatile-rich or oxygen-rich core. *Earth and Planetary*  
358 *Science Letters*, 473, 94–103. <https://doi.org/10.1016/j.epsl.2017.05.024>
- 359 Mori, Y., Ozawa, H., Hirose, K., Sinmyo, R., Tateno, S., Morard, G., & Ohishi, Y. (2017).  
360 Melting experiments on Fe–Fe<sub>3</sub>S system to 254 GPa. *Earth and Planetary Science*  
361 *Letters*, 464, 135–141. <https://doi.org/10.1016/j.epsl.2017.02.021>
- 362 Nomura, R., Hirose, K., Uesugi, K., Ohishi, Y., Tsuchiyama, A., Miyake, A., & Ueno, Y.  
363 (2014). Low core-mantle boundary temperature inferred from the solidus of pyrolite.  
364 *Science*, 343, 522–525. <https://doi.org/10.1126/science.1248186>
- 365 Oka, K., Hirose, K., Tagawa, S., Kidokoro, Y., Nakajima, Y., Kuwayama, Y., et al. (2019).  
366 Melting in the Fe-FeO system to 204 GPa: implications for oxygen in Earth's core.  
367 *American Mineralogist*, 104, 1603–1607. <https://doi.org/10.2138/am-2019-7081>
- 368 Olson, P. L., & Sharp, Z.D. (2019). Nebular atmosphere to magma ocean: a model for  
369 volatile capture during Earth accretion. *Physics of the Earth and Planetary Interiors*,  
370 294, 106294. <https://doi.org/10.1016/j.pepi.2019.106294>
- 371 Ozawa, H., Hirose, K., Tateno, S., Sata, N., & Ohishi, Y. (2010). Phase transition  
372 boundary between B1 and B8 structures of FeO up to 210GPa. *Physics of the Earth*  
373 *and Planetary Interiors*, 179, 157–163. <https://doi.org/10.1016/j.pepi.2009.11.005>

374 Raymond, S. N., Quinn, T., & Lunine, J. I. (2007). High-resolution simulations of the  
375 final assembly of Earth-like planets. 2. Water delivery and planetary habitability.  
376 *Astrobiology*, 7, 66–84. <https://doi.org/10.1089/ast.2006.06-0126>.

377 Sakai, F., & Hirose, K. (2021). Melting experiments on the Fe-C-O ternary system under  
378 core pressures. JpGU Meeting Abstract

379 Sakamaki, K., Takahashi, E., Nakajima, Y., Nishihara, Y., Funakoshi, K., Suzuki, T., &  
380 Fukai, Y. (2009). Melting phase relation of FeH<sub>x</sub> up to 20 GPa: implication for the  
381 temperature of the Earth's core. *Physics of the Earth and Planetary Interiors*, 174,  
382 192–201. <https://doi.org/10.1016/j.pepi.2008.05.017>

383 Seagle, C. T., Heinz, D. L., Campbell, A. J., Prakapenka, V. B., & Wanless, S. T. (2008).  
384 Melting and thermal expansion in the Fe-FeO system at high pressure. *Earth and*  
385 *Planetary Science Letters*, 265, 655–665. <https://doi.org/10.1016/j.epsl.2007.11.004>

386 Scheler, T., Degtyareva, O., & Gregoryanz, E. (2011). On the effects of high temperature  
387 and high pressure on the hydrogen solubility in rhenium. *Journal of Chemical Physics*,  
388 135, 214501. <https://doi.org/10.1063/1.3652863>

389 Shibazaki, Y., Terasaki, H., Ohtani, E., Tateyama, R., Nishida, K., Funakoshi, K., & Higo,  
390 Y. (2014). High-pressure and high-temperature phase diagram for Fe<sub>0.9</sub>Ni<sub>0.1</sub>-H alloy.  
391 *Physics of the Earth and Planetary Interiors*, 228, 192–201.  
392 <https://doi.org/10.1016/j.pepi.2013.12.013>

393 Stixrude, L. (2012). Structure of iron to 1 Gbar and 40 000 K. *Physical Review Letters*,  
394 108, 055505. <https://doi.org/10.1103/PhysRevLett.108.055505>

395 Tagawa, S., Gomi, H., Hirose, K., & Ohishi, Y. (2021). High-temperature equation of  
396 state of FeH: implications for hydrogen in Earth's inner core. *Earth and Space Science*  
397 *Open Archive*. <https://doi.org/10.1002/essoar.10508224.1>

398 Tagawa, S., Sakamoto, N., Hirose, K., Yokoo, S., Hernlund, J., Ohishi, Y., & Yurimoto,  
399 H. (2021). Experimental evidence for hydrogen incorporation into Earth's core. *Nature*  
400 *Communications*, 12, 2588. <https://doi.org/10.1038/s41467-021-22035-0>

401 Tateno, S., Hirose, K., Sinmyo, R., Morard, G., Hirao, N., & Ohishi, Y. (2018). Melting  
402 experiments on Fe–Si–S alloys to core pressures: silicon in the core? *American*  
403 *Mineralogist*, 103, 742–748. <https://doi.org/10.2138/am-2018-6299>

404 Thompson, E. C., Davis, A. H., Bi, W., Zhao, J., Alp, E. E., Zhang, D., et al. (2018). High-  
405 pressure geophysical properties of fcc phase FeH<sub>x</sub>. *Geochemistry, Geophysics,*  
406 *Geosystems*, 19, 305–314. <https://doi.org/10.1002/2017GC007168>

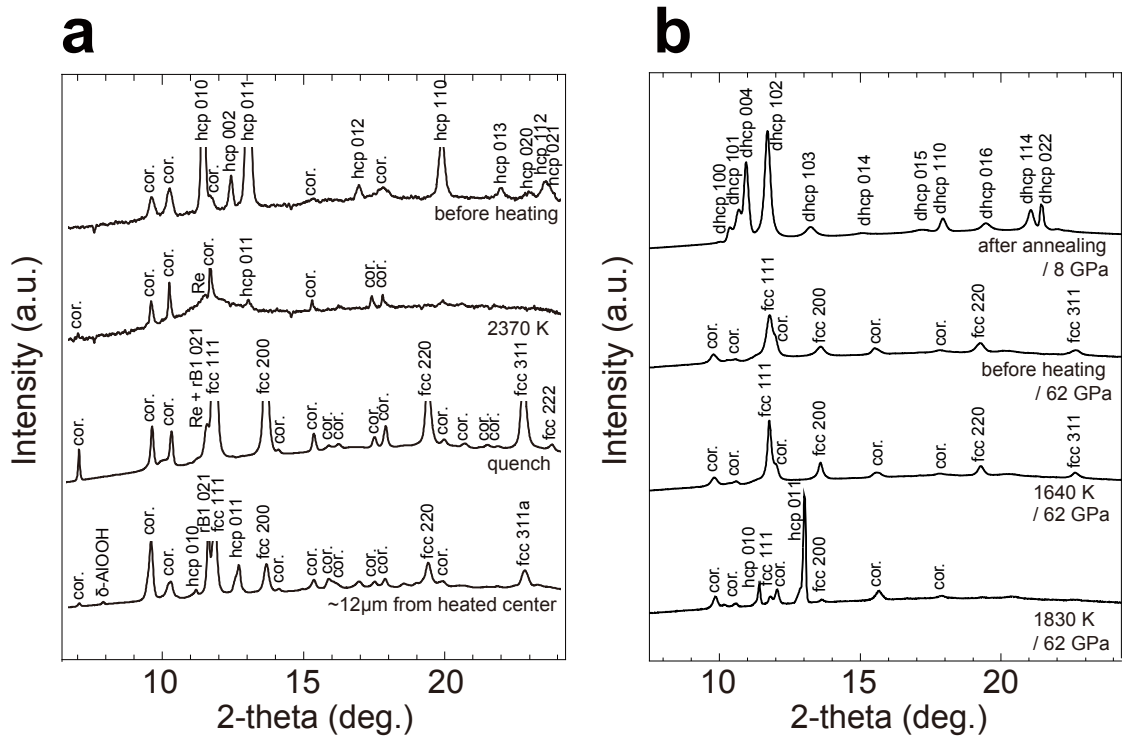
407 Umemoto, K., & Hirose, K. (2015). Liquid iron-hydrogen alloys at outer core conditions  
408 by first-principles calculations. *Geophysical Research Letters*, 42, 7513–7520.  
409 <https://doi.org/10.1002/2015GL065899>

- 410 Umemoto, K., & Hirose, K. (2020). Chemical compositions of the outer core examined  
411 by first principles calculations. *Earth and Planetary Science Letters*, 531, 116009.  
412 <https://doi.org/10.1016/j.epsl.2019.116009>
- 413 Vočadlo, L., Alfè, D., Gillan, M. J., & Price, G. D. (2003). The properties of iron under  
414 core conditions from first principles calculations. *Physics of the Earth and Planetary*  
415 *Interiors*, 140, 101–125. <https://doi.org/10.1016/j.pepi.2003.08.001>
- 416 Walsh, K. J., Morbidelli, A., Raymond, S. N., O'brien, D. P., & Mandell, A. M. (2011). A  
417 low mass for Mars from Jupiter's early gas-driven migration. *Nature*, 475, 206–209.  
418 <https://doi.org/10.1038/nature10201>
- 419 Wang, W., Li, Y., Brodholt, J. P., Vočadlo, L., Walter, M. J., & Wu, Z. (2021). Strong shear  
420 softening induced by superionic hydrogen in Earth's inner core. *Earth and Planetary*  
421 *Science Letters*, 568, 117014. <https://doi.org/10.1016/j.epsl.2021.117014>
- 422 Yokoo, S., Hirose, K., Sinmyo, R., & Tagawa, S. (2019). Melting experiments on liquidus  
423 phase relations in the Fe-S-O ternary system under core pressures. *Geophysical*  
424 *Research Letters*, 46, 5137–5145. <https://doi.org/10.1029/2019GL082277>
- 425 Yuan, L., & Steinle-Neumann, G. (2020). Strong sequestration of hydrogen into the  
426 Earth's core during planetary differentiation. *Geophysical Research Letters*, 47,  
427 e2020GL088303. <https://doi.org/10.1029/2020GL088303>

## 428 **References From the Supporting Information**

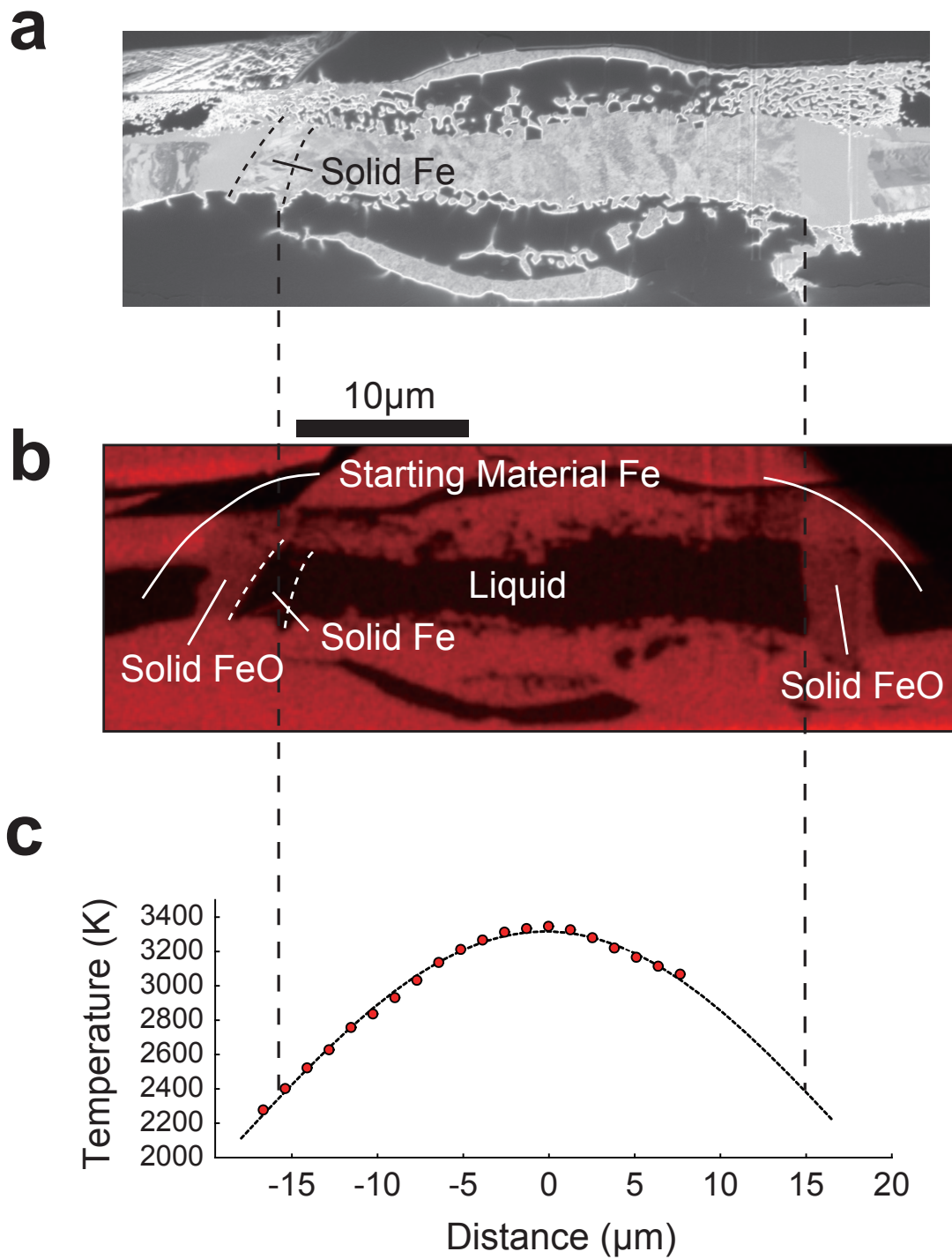
- 429 Akahama, Y., & Kawamura, H. (2004). High-pressure Raman spectroscopy of diamond  
430 anvils to 250 GPa: method for pressure determination in the multimegabar pressure  
431 range. *Journal of Applied Physics*, 96, 3748–3751. <https://doi.org/10.1063/1.1778482>
- 432 Badro, J., Siebert, J., & Nimmo, F. (2016). An early geodynamo driven by exsolution of  
433 mantle components from Earth's core. *Nature*, 536, 326–328.  
434 <https://doi.org/10.1038/nature18594>
- 435 Caracas, R. (2015). The influence of hydrogen on the seismic properties of solid iron.  
436 *Geophysical Research Letters*, 42, 3780–3785.  
437 <https://doi.org/10.1002/2015GL063478>
- 438 Chi, Z., Nguyen, H., Matsuoka, T., Kagayama, T., Hirao, N., Ohishi, Y., & Shimizu, K.  
439 (2011). Cryogenic implementation of charging diamond anvil cells with H<sub>2</sub> and D<sub>2</sub>.  
440 *Review of Scientific Instruments*, 82, 105109. <https://doi.org/10.1063/1.3652981>
- 441 Dewaele, A., & Torrent, M. (2013). Equation of state of  $\alpha$ -Al<sub>2</sub>O<sub>3</sub>. *Physical Review B*, 88,  
442 064107. <https://doi.org/10.1103/PhysicalReviewB.88.064107>

443 Dewaele, A. S., Loubeyre, P., Occelli, F., Mezouar, M., Dorogokupets, P. I., & Torrent,  
444 M. (2006). Quasihydrostatic equation of state of iron above 2 Mbar. *Physical Review*  
445 *Letters*, *97*, 215504. [https://doi.org/10.1103/Physical Review Letters.97.215504](https://doi.org/10.1103/PhysicalReviewLetters.97.215504)  
446 Dorogokupets, P. I., Dymshits, A. M., Litasov, K. D., & Sokolova, T. S. (2017).  
447 Thermodynamics and equations of state of iron to 350 GPa and 6000 K. *Scientific*  
448 *Reports*, *7*, 41863. <https://doi.org/10.1038/srep41863>  
449 Helffrich, G. (2014). Outer core compositional layering and constraints on core liquid  
450 transport properties. *Earth and Planetary Science Letters*, *391*, 256–262.  
451 <https://doi.org/10.1016/j.epsl.2014.01.039>  
452 Helffrich, G., Hirose, K., & Nomura, R. (2020). Thermodynamical modeling of liquid Fe-  
453 Si-Mg-O: molten magnesium silicate release from the core. *Geophysical Research*  
454 *Letters*, *47*, e2020GL089218. <https://doi.org/10.1029/2020GL089218>  
455 Hirao, N., Kawaguchi, S. I., Hirose, K., Shimizu, K., Ohtani, E., & Ohishi, Y. (2020).  
456 New developments in high-pressure X-ray diffraction beamline for diamond anvil cell  
457 at SPring-8. *Matter and Radiation at Extremes*, *5*, 018403.  
458 <https://doi.org/10.1063/1.5126038>  
459 Hirose, K., Tagawa, S., Kuwayama, Y., Sinmyo, R., Morard, G., Ohishi, Y., & Genda, H.  
460 (2019). Hydrogen limits carbon in liquid iron. *Geophysical Research Letters*, *46*,  
461 5190–5197. <https://doi.org/10.1029/2019GL082591>  
462 Iizuka-Oku, R., Yagi, T., Gotou, H., Okuchi, T., Hattori, T., & Sano-Furukawa, A. (2017).  
463 Hydrogenation of iron in the early stage of Earth’s evolution. *Nature Communications*,  
464 *8*, 14096. <https://doi.org/10.1038/ncomms14096>  
465 Ikuta, D., Ohtani, E., Sano-Furukawa, A., Shibazaki, Y., Terasaki, H., Yuan, L., & Hattori,  
466 T. (2019). Interstitial hydrogen atoms in face-centered cubic iron in the Earth’s core.  
467 *Scientific Reports*, *9*, 7108. <https://doi.org/10.1038/s41598-019-43601-z>  
468 Ohta, K., Ichimaru, K., Einaga, M., Kawaguchi, S., Shimizu, K., Matsuoka, T., et al.  
469 (2015). Phase boundary of hot dense fluid hydrogen. *Scientific Reports*, *5*, 16560.  
470 <https://doi.org/10.1038/srep16560>  
471 Seto, Y., Nishio-Hamane, D., Nagai, T., & Sata, N. (2010). Development of a software  
472 suite on X-ray diffraction experiments. *The Review of High Pressure Science and*  
473 *Technology*, *20*, 269–276  
474



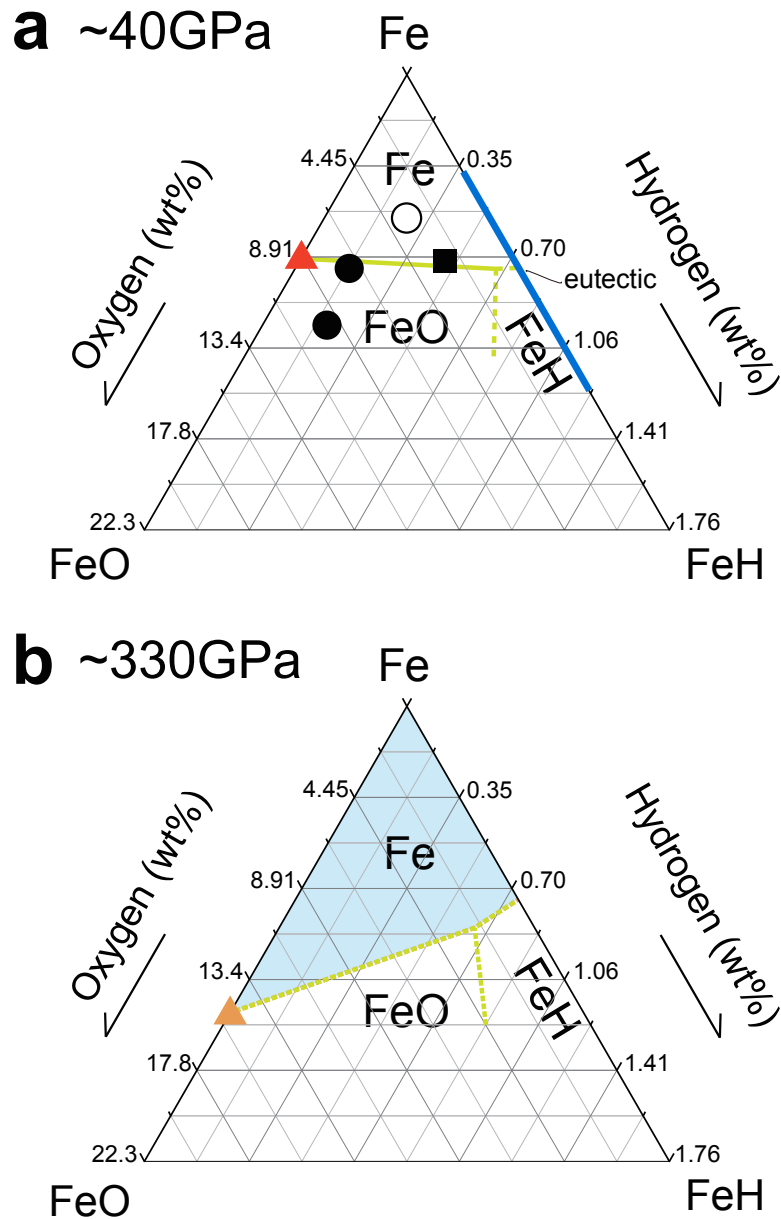
475

476 **Figure 1.** XRD patterns collected in (a) run #A4 for the Fe-O-H sample at ~40 GPa and  
 477 (b) run #B for the Fe-H sample at ~62 GPa. Hcp, hcp FeH<sub>x</sub>; fcc, fcc FeH<sub>x</sub>; dhcp, FeH;  
 478 rB1, rhombohedral B1 FeO; cor, corundum (pressure medium); Re, rhenium (gasket). In  
 479 (b), fcc FeH<sub>0.77</sub> at 1640 K dissociated into hcp FeH<sub>0.21</sub> and fcc FeH<sub>0.69</sub> with increasing  
 480 temperature to 1830 K.



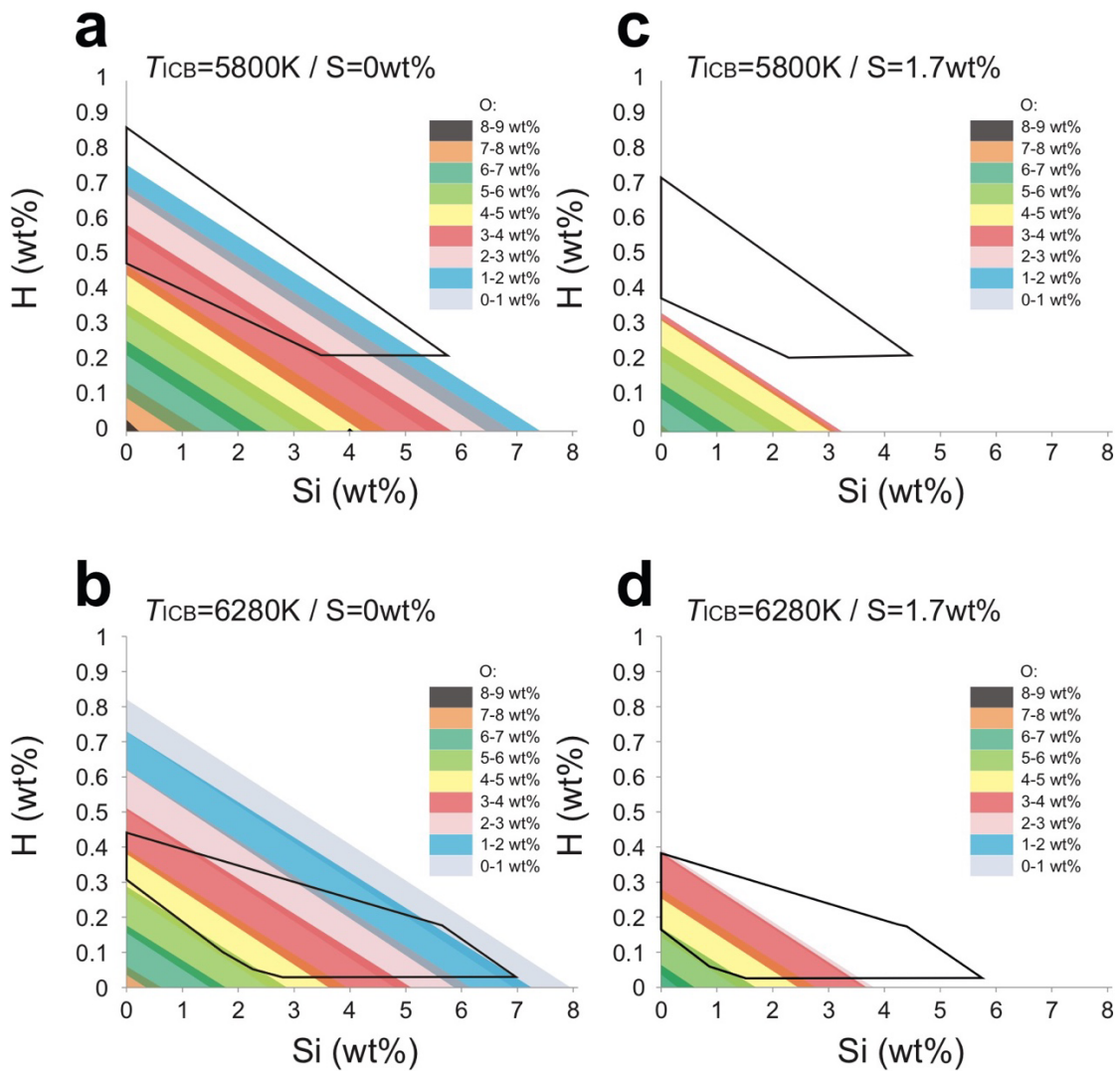
481

482 **Figure 2.** Sample cross sections and temperature profile in run #A4. Scanning ion  
 483 microscope image (a) and X-ray map of oxygen (b) show that liquid coexisted with solid  
 484 Fe and FeO. Temperature at the liquid/solid boundary is obtained by a combination of  
 485 these images and a temperature profile (c).



486

487 **Figure 3.** Liquidus phase diagrams of the Fe-FeO-FeH ternary system. Green lines are  
 488 cotectic lines that separate the liquidus fields of Fe, FeO, and FeH. In (a) for ~40 GPa,  
 489 circles and square show the compositions of liquids coexisting with FeO and Fe + FeO,  
 490 respectively (filled and open symbols indicate 0.1–0.4 wt% and 1.7 wt% C in liquids,  
 491 respectively). A blue bar shows the solid miscibility gap in the Fe-FeH system observed  
 492 in run #B. The Fe-FeO eutectic liquid composition is given by a red triangle from [Figure](#)  
 493 [S1](#). The Fe-FeH eutectic liquid composition may be FeH<sub>0.42</sub> (Fe + 0.75 wt% H). (b) The  
 494 liquidus phase relations extrapolated to 330 GPa considering the Fe-FeO (orange triangle,  
 495 [Figure S1](#)) and Fe-FeH binary eutectic liquid compositions (the latter could exhibit little  
 496 pressure dependence). The liquidus field of Fe is illustrated by a blue area.



497

498 **Figure 4.** Possible ranges of the outer core liquid composition in the Fe-O-Si-H±1.7wt%S  
 499 system. Colored areas show liquid compositions that are compatible with the observed  
 500 outer core density and P-wave velocity (Umemoto & Hirose, 2020) and within the  
 501 liquidus field of Fe. The areas enclosed by black lines indicate liquid compositions that  
 502 are in equilibrium with the possible compositions of the inner core solid that explain  
 503 observed density, P- and S-wave velocities (Li et al., 2018; Wang et al., 2021).  
 504

505



506

507

*Geophysical Research Letters*

508

Supporting Information for

509

**Melting Experiments on Fe-O-H: Evidence for Eutectic Melting in Fe-FeH and  
Implications for Hydrogen in the Core**

510

511

512

Kenta Oka<sup>1</sup>, Shoh Tagawa<sup>1,2</sup>, Kei Hirose<sup>1,2</sup>, and Yasuo Ohishi<sup>3</sup>

513

514

<sup>1</sup>Department of Earth and Planetary Science, The University of Tokyo, Bunkyo, Tokyo, Japan

515

<sup>2</sup>Earth-Life Science Institute, Tokyo Institute of Technology, Meguro, Tokyo, Japan

516

<sup>3</sup>Japan Synchrotron Radiation Research Institute, SPring-8, Sayo, Hyogo, Japan

517

518

**Contents of this file**

519

Experimental Methods

520

Tables S1, S2

521

Figure S1

522

## 523 **Experimental Methods**

524 **Melting experiments on the Fe-O-H system.** We used diamond anvils with flat 300  
525  $\mu\text{m}$  or single-beveled 120  $\mu\text{m}$  culet size for experiments on Fe-O $\pm$ H (Table S1). A pure  
526 Fe (5N, Mairon-UHP, Toho Zinc) or Fe-12wt%O foil, same as that used in Oka et al.  
527 (2019), was loaded into a hole at the center of a pre-indented rhenium gasket, together  
528 with a powder mixture of Al(OH)<sub>3</sub> and Al<sub>2</sub>O<sub>3</sub> (a source of oxygen and hydrogen) and 10  
529  $\mu\text{m}$ -thick Al<sub>2</sub>O<sub>3</sub> sapphire single crystals (thermal insulation layers). Upon heating,  
530 Al(OH)<sub>3</sub> dehydrates to form AlOOH or Al<sub>2</sub>O<sub>3</sub>. The mixing ratio between Al<sub>2</sub>O<sub>3</sub> and  
531 Al(OH)<sub>3</sub> was varied in order to change the Fe/H<sub>2</sub>O ratio of a system.

532 The sample was heated from both sides with a couple of 100W single-mode Yb fiber  
533 lasers with flat-top beam-shaping optics. The laser spot size was 20–30  $\mu\text{m}$  across. The  
534 heating duration was limited to less than 3 sec to avoid temperature fluctuations which  
535 could lead to a complex melting texture. Indeed, it is long enough for O and H to diffuse  
536 over a melt pocket (Helffrich, 2014), which assures chemical equilibrium between liquid  
537 and solid when considering that melting/crystallization at the liquid-solid boundary  
538 occurs almost instantaneously (Yokoo et al., 2019; Hasegawa et al., 2021). According to  
539 previous time-series melting experiments on the Fe-S system, the compositions of  
540 coexisting liquid and solid did not change after heating for 1 sec in a laser-heated DAC  
541 (Mori et al., 2017). The diffusivities of O and H in molten iron are higher than that of S  
542 (Helffrich, 2014). A temperature profile was obtained using a spectro-radiometric method  
543 (Hirao et al., 2020). The temperature at the liquid/solid boundary corresponds to the  
544 liquidus temperature of a liquid obtained in each run. We determined it by combining the  
545 temperature profile with a sample cross-section (e.g., Mori et al., 2017; Tateno et al.,  
546 2018; Oka et al., 2019) (Figure 2c).

547 We performed XRD measurements in-situ at high  $P$ - $T$  using an X-ray beam with energy  
548 of  $\sim$ 30 keV at the beamline BL10XU, SPring-8 (Figure 1). XRD spectra were collected  
549 on a flat panel detector (FPD, Perkin Elmer) with exposure time of 1 sec before and after  
550 heating at 300 K and of 0.2 sec continuously during laser heating. The IPAnalyzer  
551 software (Seto et al., 2010) was used to integrate two-dimensional XRD image into one-  
552 dimensional diffraction profile. Sample pressure was measured at 300 K after heating  
553 based on the unit-cell volume of Al<sub>2</sub>O<sub>3</sub> corundum and its equation of state (Dewaele &  
554 Torrent, 2013). We considered that 60% and 90% of theoretical thermal pressure for  
555 purely isochoric heating,  $\Delta P = \alpha K_T \times (T - 300)$  ( $\alpha K_T = 4$  and 9 MPa/K), contributed to an  
556 increase in sample pressure during heating at  $\sim$ 40 GPa and  $\sim$ 150 GPa, respectively (e.g.,  
557 Hirose et al., 2019; Oka et al., 2019).

558 Textural and chemical characterizations except for H (see below) were carried out on each  
 559 recovered sample; it is well known that H escapes from metal Fe when it transforms into  
 560 bcc during decompression (e.g., Iizuka-Oku et al., 2017; Tagawa, Sakamoto et al., 2021).  
 561 A sample cross-section and X-ray elemental maps were obtained parallel to the  
 562 compression axis by a focused ion beam (FIB, *FEI Versa 3D DualBeam*) and an energy-  
 563 dispersive spectroscopy (EDS) attached to a field-emission (FE)-type scanning electron  
 564 microscope (SEM) (Figures 2a, b). Quantitative chemical analyses were then made for  
 565 coexisting liquid and crystals (liquidus phases) with an FE-type electron probe micro-  
 566 analyzer (FE-EPMA, *JEOL JXA-8530F*) with an accelerating voltage of 12 kV, a current  
 567 of 15 nA, and the X-ray counting time of 20/10 sec for peak/background. Fe, Fe<sub>3</sub>C, and  
 568 corundum were used as standards. LIF (Fe), LDE2H (C), TAP (Al), and LDE1 (O) were  
 569 analyzing crystals. The FE-EPMA analyses of quenched liquid Fe sometimes included a  
 570 small amount of Al, which is likely a signal from the surrounding pressure medium or  
 571 Al<sub>2</sub>O<sub>3</sub> grains that mechanically intruded into the liquid; note that the amount of Al  
 572 incorporated into liquid Fe metal is negligible (Badro et al., 2016; Helffrich et al., 2020).  
 573 Al was therefore subtracted as Al<sub>2</sub>O<sub>3</sub> from raw data. C was detected not only in the  
 574 quenched liquid but also inside the rhenium gasket; the latter could be due to  
 575 contamination during FIB and/or FE-EPMA analysis. Thus, we subtracted 0.2–0.4 wt%  
 576 C from the raw analyses of liquids, which was found on the rhenium gasket in the same  
 577 sample cross-section. The liquid should have included the remaining 0.1–3.7 wt% C  
 578 (Table S1).

579 H concentration,  $x$  in FeH <sub>$x$</sub> , was estimated from its lattice volume (Hirose et al., 2019;  
 580 Tagawa, Sakamoto et al., 2021), which expands proportionally to the H content (Caracas,  
 581 2015);

$$582 \quad x = \frac{V_{\text{FeH}_x} - V_{\text{Fe}}}{\Delta V_{\text{H}}}, \quad (1)$$

583 where  $V_{\text{FeH}_x}$  and  $V_{\text{Fe}}$  are the unit-cell volumes of FeH <sub>$x$</sub>  and Fe (Dorogokupets et al., 2017  
 584 for fcc Fe and Dewaele et al., 2006 for hcp Fe), respectively, and  $\Delta V_{\text{H}}$  is an increase in  
 585 the lattice volume of Fe per H atom from Caracas (2015). The error in the H content,  $x$ ,  
 586 is estimated to be  $\pm 8\%$  at maximum, which is mainly derived from uncertainty in  $\Delta V_{\text{H}}$   
 587 (Ikuta et al., 2019; Tagawa, Sakamoto et al., 2021).

588 **Subsolidus experiment on Fe-H.** We have also conducted an experiment on the Fe-  
 589 FeH binary system (Table S2), using a laser-heated DAC with beveled 200  $\mu\text{m}$  culet anvil.  
 590 A 10- $\mu\text{m}$  thick pure iron foil was loaded between the disks of Al<sub>2</sub>O<sub>3</sub> single crystals. A

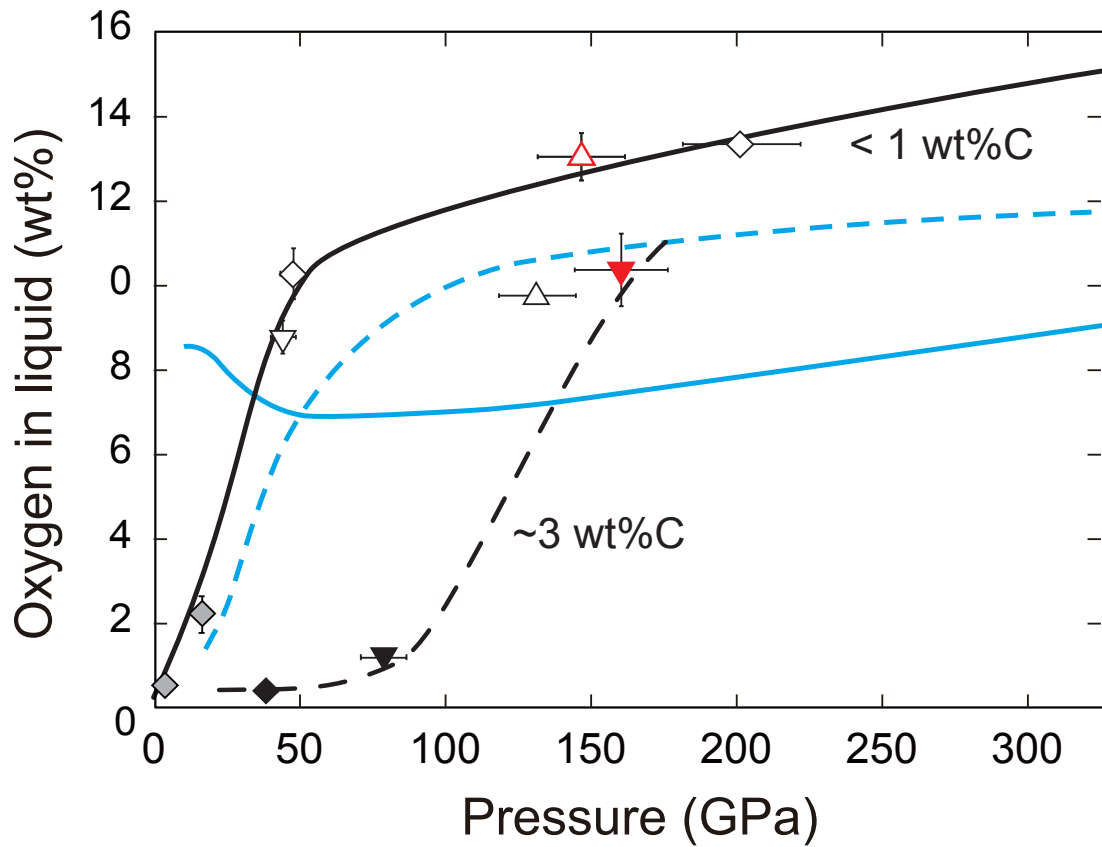
591 whole DAC was dried in a vacuum oven at 393 K for at least one hr and subsequently at  
592 350 K for 30 mins in a vacuumed hydrogen-loading system.

593 Hydrogen was cryogenically loaded into a sample chamber (Chi et al., 2011). After the  
594 chamber was filled with liquid H, sample was compressed at ~15 K and then restored to  
595 room temperature. The surface of the diamond anvils was coated with a thin layer of Ti  
596 by sputtering (Ohta et al., 2015) in order to avoid anvil failure. FeH<sub>x</sub> was synthesized by  
597 thermal annealing with a laser at 8 GPa. Upon compression to 23 GPa, excess molecular  
598 H<sub>2</sub> in the sample chamber was lost to a neighboring rhenium gasket to form ReH<sub>x</sub> (Scheler  
599 et al., 2011). We heated the FeH<sub>x</sub> sample at 62 GPa with in-situ XRD measurements at  
600 BL10XU, SPring-8 (Figure 1b). We obtained pressures of 8 and 23 GPa from the Raman  
601 shift of a diamond anvil (Akahama & Kawamura, 2004) and those at 62 GPa based on  
602 the lattice volume of Al<sub>2</sub>O<sub>3</sub> corundum (Dewaele & Torrent, 2013). Other procedures  
603 including the determination of the H contents in solid Fe phases were similar to those for  
604 the Fe-O±H sample described above.

605



615



616

617 **Figure S1.** Liquid compositions obtained in melting experiments on the Fe-FeO±C  
618 system. Normal and reverse triangles, lower and upper bounds for O concentration in the  
619 Fe-FeO eutectic liquid, respectively; diamonds, the O contents in liquids coexisting both  
620 Fe and FeO (eutectic liquids). Red, this study (runs #A5 and #A6); black, Oka et al.  
621 (2019); gray, Ohtani et al. (1984) and Ringwood & Hibberson (1990). The black curves  
622 indicate changes in O concentration in liquids coexisting with Fe and FeO (solid line,  
623 with <1 wt% C in liquids; broken line, with ~3 wt% C in liquids). Blue dashed and solid  
624 curves represent thermodynamically-modelled eutectic liquid compositions in the Fe-  
625 FeO system assuming non-ideal and ideal solutions, respectively (Komabayashi, 2014).